Atomically thin quantum light emitting diodes

Carmen Palacios Berraquero[1], Matteo Barbone[2], Dhiren M. Kara[1], Xiaolong Chen[2], Ilya Goykhman[2], Duhee Yoon[2], Anna K. Ott[2], Jan Beitner[1], Kenji Watanabe[3], Takashi Taniguchi[3], Andrea C. Ferrari[2†] and Mete Atatüre[1*]

[1]*Cavendish Laboratory, University of Cambridge, JJ Thomson Ave., Cambridge CB3 0HE, UK*

[2]*Cambridge Graphene Centre, University of Cambridge, Cambridge CB3 0FA, UK*

[3]*Advanced Materials Laboratory, National Institute for Materials Science, Tsukuba, Ibaraki 305-0034, Japan*

Transition metal dichalcogenides (TMDs) are optically active layered materials providing potential for fast optoelectronics and on-chip photonics. We demonstrate electrically driven single-photon emission from localised sites in tungsten diselenide (WSe_2) and tungsten disulphide (WS_2). To achieve this, we fabricate a light emitting diode structure comprising single layer graphene, thin hexagonal boron nitride and TMD mono- and bi-layers. Photon correlation measurements are used to confirm the single-photon nature of the spectrally sharp emission. These results present the TMD family as a platform for hybrid, broadband, atomically precise quantum photonics devices.

Integrating single-photon sources into optoelectronic circuits is a key challenge to develop scalable quantum-photonic technologies. Despite a plethora of single-photon sources reported to-date, all-electrical operation, critical for systems integration, is reported for only three systems [1–3]. Layered materials (LMs) offer novel opportunities for next-generation photonic and optoelectronic technologies [4,5], such as lasers [6,7], modulators [8,9] and photodetectors [10], and show great promise for integration into the silicon platform [11]. Here, we demonstrate that LMs enable all-electrical single-photon generation over a broad spectrum. We use a light emitting diode (LED) realised by vertical stacking of LMs and achieve charge injection into the active layer containing quantum emitters. We demonstrate that quantum emitters in tungsten diselenide (WSe_2) [12–16] can operate electrically. We further report all-electrical single-photon generation in the visible spectrum from a new class of quantum emitters in tungsten disulphide (WS_2). Our results highlight the promise of LMs as a new platform for broadband hybrid all-integrated quantum-photonic circuits.

The attractiveness of single-photon sources in LMs [12–17] stems from their ability to operate at the fundamental limit of few-atom thickness, providing the potential to integrate into conventional and scalable high-speed optoelectronic systems [18,19]. This is in stark contrast to any other quantum emitter system hosted in semiconductors or diamond that we know today, since these suffer from any proximity to an interface. Transition metal dichalcogenides (TMDs), being optically active layered semiconductors, are particularly suitable to develop integrable devices for quantum-light generation. With this in mind, we realise an LED based on a single tunnelling junction made of vertically stacked LMs (see Appendix). Figure 1a is a typical optical microscope image of such a device. From bottom to top, three layers form a heterostructure on a silicon/silicon dioxide (Si/SiO_2) substrate: A single layer of graphene (SLG), a thin (2-6 atomic layers) sheet of hexagonal boron nitride (hBN), and finally a mono- or bilayer of TMD, such as WSe_2. The WSe_2, exfoliated from a naturally p-doped bulk crystal, is the optically active layer hosting single-photon sources. Metal electrodes provide electrical contact to the SLG and TMD layers. To obtain electroluminescence (EL), we inject electrons from the SLG to the p-doped WSe_2 through the hBN tunnel barrier (see Appendix for current-voltage characteristics of the devices). A

vertically stacked heterojunction allows for EL from the whole device area, unlike lateral Schottky junction or split-gate p-n junction devices [20–22], and provides the benefit of atomically precise interfaces and barrier thicknesses [23]. We leave the optically active TMD layer exposed at the top of the device purposefully to offer interfacing with other systems.

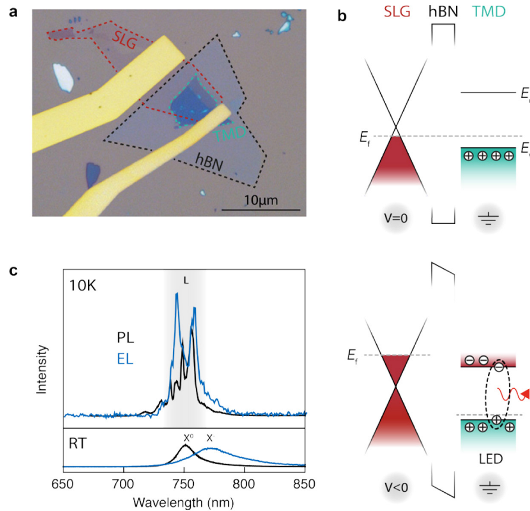

FIG. 1. a, Optical microscope image of a typical device used in our experiments. The dotted lines highlight the footprint of the SLG, hBN and the TMD layers individually. The Cr/Au electrodes contact the SLG and TMD layers to provide an electrical bias. **b,** Heterostructure band diagram. The top illustration shows the case for zero applied bias and the bottom illustration shows the case for a finite negative bias applied to the SLG. Tuning the SLG E_F across the conduction band of the TMD allows electron tunnelling from SLG to TMD resulting in light emission via radiative recombination of the electrons with the resident holes in the p-doped TMD layer. **c,** An example of layered LED emission spectra for an optically active layer of WSe_2. Top (bottom) spectra correspond to 10 K (RT) operation temperature, where the black and blue spectra are obtained by optical excitation and electrical excitation, respectively.

Figure 1b illustrates the operational concept of our LED. At zero bias between the SLG and the monolayer TMD contacts, the Fermi energy (E_F) of the system is constant across the heterojunction, preventing net charge flow (current) between the layers (Fig. 1b, top). A negative bias applied to the SLG electrode raises the SLG E_F above the minimum of the conduction band (E_C) of grounded WSe_2 and thus electrons tunnel from the SLG into the monolayer WSe_2. This initiates photoemission through radiative recombination between the tunnelled electrons and the holes residing in the optically active WSe_2 area (Fig. 1b, bottom). Figure 1c compares the EL and photoluminescence (PL) spectra from this monolayer-WSe_2-based LED device for two operation temperatures, room temperature (RT) and 10 K (see Appendix for measurement setup). PL at RT is given by the black curve in the lower panel with a broad peak at 750 nm corresponding to the monolayer WSe_2 unbound neutral exciton emission, X^0 [24]. Under electrical excitation the main peak is shifted ~20 nm to longer wavelengths, which is commensurate with the charged exciton, X^- [25], as shown in the blue curve. The black and blue spectra in the upper panel of Fig. 1c show the device's PL and EL emission at 10 K, respectively. Due to the increased bandgap at low temperatures, the unbound exciton emission is shifted to shorter wavelengths by ~30 nm [26]. Consistent with recent reports [12–16,26], extra structure arising from localised exciton state emission (L) appears at longer wavelengths in the PL spectrum. Critically, these features are also visible under electrical excitation. In the low current regime (<1 μA for this device) they dominate the EL spectrum, as shown in Fig. 1c, indicating that localised exciton states respond more efficiently to charge injection than the delocalised ones.

Figure 2a is a spatial map of integrated EL from a WSe_2-based LED device at 10K. The active region of this device consists of adjacent monolayer and bilayer active areas, both in contact with the ground electrode. The brighter area in Fig. 2a corresponds to the bilayer, suggesting that most of the injected current flows through this region (see Appendix). In addition to the spatially uniform light emission from delocalised excitons, we observe quantum LED (QLED) operation in the form of highly localised light emission from both the monolayer and the bilayer WSe_2, identified by the dotted circles (Fig. 2a). These localised states lie within the

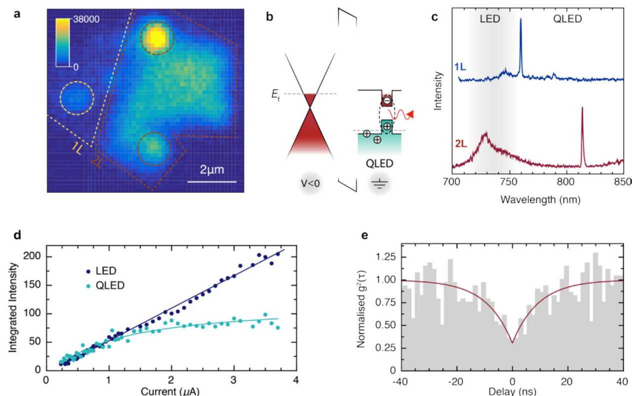

FIG. 2. a, A raster-scan map of integrated EL intensity from monolayer and bilayer WSe_2 areas of layered QLED for an injection current of 3 μA (12.4 V). The dotted circles highlight the sub-micron localised emission in this device. **b,** A schematic energy band diagram, similar to that in Fig. 1b, including the confined (and lower energy) electronic states for the quantum dots. EL emission from quantum dots typically starts at lower bias than the conventional LED operation threshold. **c,** Typical EL emission spectra for quantum dots in monolayer (top) and bilayer (bottom) WSe_2. The shaded area highlights the spectral window for LED emission due to bulk WSe_2 excitons, while QLED operation produces spectra at longer wavelengths. **d,** Comparison of the integrated EL intensity for the WSe_2 layer and for a quantum dot as a function of the applied current. The linear increase in WSe_2 layer EL contrasts with the saturation behaviour of the QLED emission. **e,** Intensity-correlation function, $g^{(2)}(\tau)$, for the same quantum dot displaying the antibunched nature of the EL signal and a radiative lifetime of 9.4±2.8 ns.

bandgap of WSe_2 and therefore emit at lower energies (longer wavelength) with respect to the bulk exciton emission (see Fig. 2b) [12–16]. Figure 2c shows example emission spectra from these sites, where the top (bottom) spectrum belongs to a quantum emitter in the monolayer (bilayer) WSe_2 section. We observe spectrally isolated peaks from various locations (and various devices) with linewidths ranging between 0.8 nm and 3 nm. Electrically excited narrow lines coming from bilayer WSe_2 regions are typically redshifted with respect to those coming from the monolayer regions [27]. The emission peaks of Fig. 2c are unpolarised, and the fine structure splitting reported in PL experiments (~0.3 nm [12–16]) is not resolvable due to the broader linewidths we observe in EL. We also see that, as in PL, the electrically driven emitters display robust operation, withstanding multiple cooling/heating cycles and several hours of measurement under uninterrupted current flow. At shorter timescales (seconds) they display a range of behaviours most likely owing to environmental effects. Most emitters show spectral wandering up to 2 nm around the transition energy, similar to that seen in our PL measurements, but remain stable as a single spectral line, whereas a fraction of the quantum emitters display blinking, discrete spectral jumps, or multiple spectral lines at similar timescales (see Appendix).

Figure 2d plots the current dependence of the integrated EL intensity from the quantum emitters, as well as the unbound monolayer WSe_2 excitons. The latter shows a predominantly linear relationship between emission intensity and injected current; however, EL emission from the quantum emitters shows clear saturation as a function of current, a universal behaviour seen with single-photon sources [28]. Figure 2e shows the measured intensity-correlation function, $g^{(2)}(\tau)$, of the integrated-EL emission from a WSe_2-based QLED using a standard Hanbury Brown and Twiss interferometer (see Appendix). The value of the normalised $g^{(2)}(0)$ drops to 0.3, well below the threshold value of 0.5 for single-photon sources [1]. We note that these data are not corrected for background emission within the spectral window of detection or for the photon-counting detector dark counts, which together contribute to the non-zero value of $g^2(0)$.

In TMD-based quantum emitters, the host material influences the quantised energy levels and, consequently their emission wavelength. Therefore, in order to obtain single-photon emission at a complementary part of the spectrum, we replace the monolayer of WSe_2 with WS_2 (exfoliated from an n-doped bulk crystal) as the active layer; the rest of the QLED device structure remains unchanged. Figures 3a and 3b display the spatial maps of integrated EL emission from a WS_2-based QLED device at high- (0.665 μA) and low- (0.570 μA) current injection, respectively. At high current, the emission intensity is spatially uniform in the monolayer. At low currents however, a localised

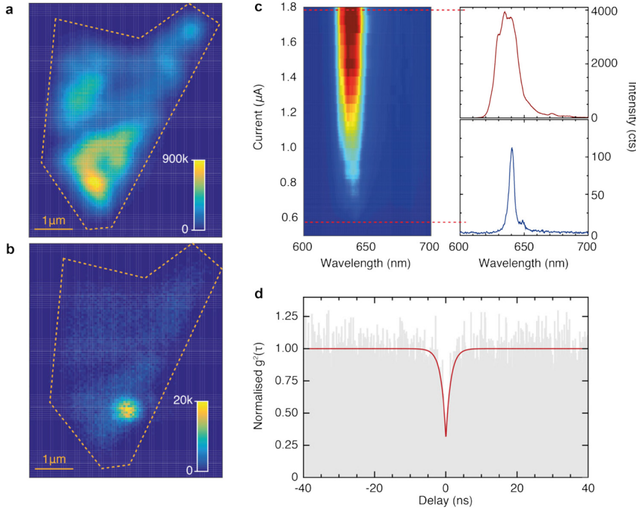

FIG. 3. a, A raster-scan map of integrated EL intensity from the monolayer WS_2 area of the layered QLED for 0.665 μA injection current (bias 2.08 V). The emission is delocalised and roughly uniform. **b,** Similar measurement as that in panel a, but for injection current of 0.570 μA (1.97 V). The WS_2 emission is not yet present, but a highly localised QLED emission is already visible at this bias. **c,** A map of the EL spectrum as a function of the applied bias displaying the evolution of the QD emission spectrum of WS_2 at high current. The spectrum at the top (bottom) of the panel is a line cut for injection current of 1.8 μA (0.578 μA). **d,** Intensity-correlation function, $g^{(2)}(\tau)$, for the same quantum dot displaying the antibunched nature of the EL signal and a radiative lifetime of 1.4±0.15 ns, an order of magnitude faster rate than the WSe_2-based quantum dots measured in such devices.

emission site dominates, indicating that WS_2 also hosts localised quantum emitters. We attribute this behaviour in part to comparatively greater oscillator strength of the localised excitons. Figure 3c shows the EL spectrum as a function of injection current, demonstrating that the low current (~0.570 μA) regime leads to a narrow (~4 nm) emission at 640 nm, a line cut (in blue) of which is in the bottom right panel. Fig. 2c (upper right plot) also shows how the EL spectrum is broadened significantly when driven strongly at an injection current of 1.8 μA. Operating in the low current range ensures that the full EL spectrum is dominated by single-photon emission from the quantum emitters obviating any need for tailored spectral filtering (see Appendix for PL spectra of the WS_2-based device). The intensity-correlation measurement for EL in this regime without spectral filtering yields the $g^{(2)}(\tau)$ data shown in Fig. 3d. Similar to the WSe_2 quantum dots, the uncorrected, but normalised, $g^{(2)}(0)$ reaches 0.26 indicating that WS_2 supports stable QLED operation generating single photons in the visible spectral range.

Our TMD-based QLEDs rely on a single tunnelling heterojunction design, where a wide range of TMDs can be active materials. Other designs, employing a back gate to tune E_F of the active TMD layer and providing electrostatic tuning of the EL emission spectrum, can enhance the versatility of these devices. Such QLEDs can further offer deterministic control over the charging states of quantum dot excitons [29], en route to spin control [30] and entangled photon generation [31]. We also note that the emission wavelength range for WSe_2 emitters can match rubidium transitions (~780 nm) for exploring quantum storage possibilities. Similarly, silicon-vacancy centres (~737 nm) and nitrogen-vacancy centres (~637 nm) in diamond can have matching transitions with the WSe_2 and WS_2 QLEDs, respectively, for interfacing hybrid quantum systems via distributed or on-chip photonic channels. Other TMDs are likely to yield similar results decorating different spectral windows. Our results offer promise to pursue these opportunities and demonstrate that layered materials are a platform for fully integrable and atomically precise devices for quantum photonics technologies.

We acknowledge financial support from the EU Graphene Flagship (no. 604391), ERC Grants Hetero2D and PHOENICS, EPSRC Grants EP/K01711X/1, EP/K017144/1, EP/N010345/1, EP/M507799/1, EP/L016087/1, EP/M013243/1 and the EPSRC Cambridge NanoDTC, EP/G037221/1. We are grateful to J. Barnes, C. Le Gall and H. S. Knowles for technical assistance.

APPENDIX

1. Materials sourcing, characterization and device assembly

We exfoliate the LMs on oxidised Si wafers by micromechanical cleavage of bulk crystals of graphite (from NGS Naturgrafit), TMDs (from HQgraphene) and hBN (hBN single crystals were grown by the temperature-gradient method under high pressure and high temperature) [32]. Mono-, bi- and few-layer samples are identified by a combination of optical contrast [33], Raman spectroscopy [34], PL, and atomic force microscopy (AFM). Single crystals are assembled into heterostructures via a dry-transfer technique [35]. A transparent stack comprising a glass slide, a polydimethylsiloxane (PDMS) layer attached to the glass and polycarbonate (PC) as an external film is mounted on a micromanipulator positioned under an optical microscope with a temperature-controlled stage. After adjusting the alignment and bringing the transfer stack into contact with the exfoliated TMD flakes, these are picked up due to their higher adhesion to PC. The process is repeated for the hBN tunnel barrier. Finally, after aligning and bringing in contact hBN and TMD on PC with exfoliated SLG on Si/SiO_2, the temperature is raised to ~100 °C, releasing the PC with hBN/TMD onto SLG. Then, the sample is soaked in Chloroform to dissolve the PC film, leaving the SLG/hBN/TMD heterostructure on the Si/SiO_2 substrate. Finally, Cr/Au (3/50 nm) contacts both to SLG and TMD are patterned by e-beam lithography following a standard lift-off process. Heterostructures are characterised by Raman spectroscopy to ensure no degradation.

We measured two sets of devices. The first consists of 1L- and 2L-WSe_2 on top of hBN on top of SLG on Si/SiO_2. We use 2L-WSe_2 in addition to 1L- to compare SPE in the two cases, as discussed in the main text. The second set has the same architecture but uses 1L-WS_2 instead of WSe_2. The crystals and heterostructures are characterised at room temperature using a combination of optical contrast, AFM, Raman spectroscopy and photoluminescence.

Optical images are acquired using a Nikon Eclipse optical microscope equipped with a 100x objective (numerical aperture 0.85). If no filter is specifically mentioned, a white light is used. AFM images are acquired using a Bruker Dimension Icon microscope in PeakForce Tapping mode. Raman and PL Spectra are

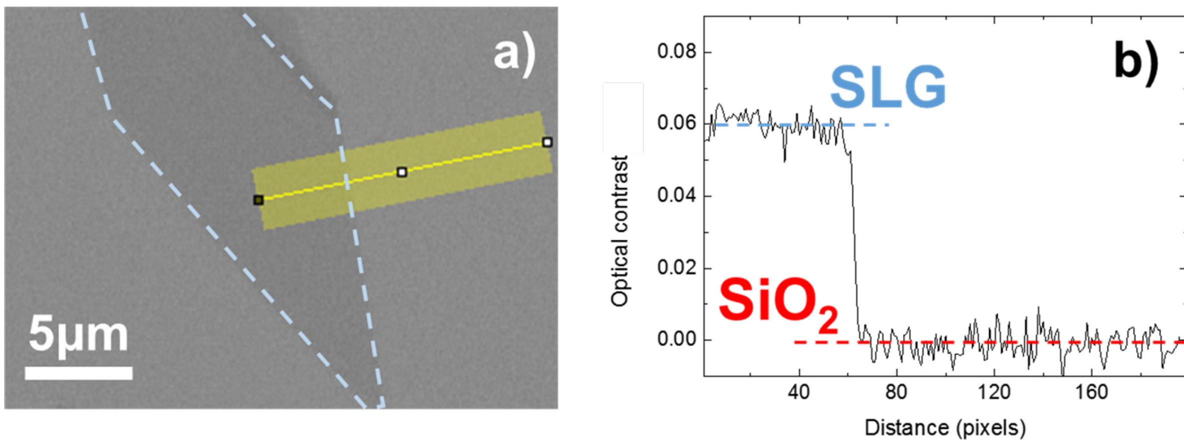

Fig. 1.1 a) optical picture of SLG on Si/SiO_2. Dashed area highlights SLG. The yellow line indicates pixels where contrast is measured. b) optical contrast along the yellow line.

acquired using a Renishaw inVia micro-spectrometer (resolution pixel-to-pixel~1.2 cm^{-1}), a 100x objective (numerical aperture 0.9) and a spot size ~1 μm. All spectra are recorded in back-scattering at 514.5 nm. The power is kept below 100 μW to prevent heating effects.

1.1 WSe_2/hBN/SLG heterostructures

The first set of devices, based on WSe_2, are assembled in a clean room as follows.

Highly oriented pyrolytic graphite (HOPG) sourced from NGS Naturgrafit is exfoliated by micromechanical cleavage [35,36] with adhesive tape (silicone-free, Ultron) and deposited on oxidised silicon wafers (oxide thickness 285 nm) to ensure good visibility[33]. SLG flakes are identified by optical contrast (Fig. 1.1) [33]. Optical contrast is calculated as $1-I_c/I_s$, where I_c is the intensity of light reflected by the flake as measured by the CCD, and I_s is the intensity of the light reflected by the substrate. In the green channel of the CCD camera, where contrast is maximum for SLG on the specific SiO_2 thickness, the optical contrast of SLG is ~6%. SLG is used as the bottom layer in the heterostructure, in contact with the Si/SiO_2 substrate on top of which it was exfoliated.

In order to build a heterostructure with clean interfaces, it is crucial to assemble the layers as soon as possible after the flakes are exfoliated. Therefore after optical contrast analysis, further characterisation is only performed after the full heterostructure is assembled.

After the exfoliation and identification of SLG, the second step consists in fabricating FL-hBN. We start from bulk hBN single crystals grown by the temperature-gradient method under high pressure and high temperature, as discussed in the main text [32].

Before exfoliation, bulk hBN crystals are characterised by Raman spectroscopy, as shown in Fig. 1.2a (orange line). The peak at ~1365.5 cm^{-1} corresponds to the E_{2g} mode of bulk hBN

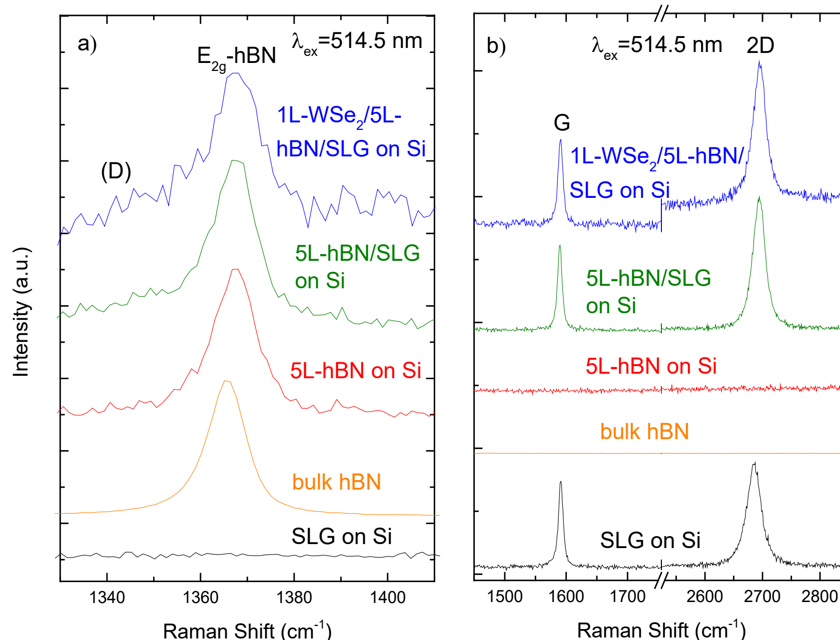

Figure 1.2: Raman spectra of SLG on Si/SiO_2 (black curve), 5L-hBN on Si/SiO_2 (red curve), 5L-hBN/SLG (green curve), and 1L-WSe_2/5L-hBN/SLG (blue curve), measured at 514.5 nm.

[37–39]. Its FWHM is ~9.2 cm^{-1}. The FWHM of hBN is linked to its crystal size according to the following equation: FWHM=1417/L_a+8.7 [37], where L_a is the hBN crystal size in Angstroms. In our case, this corresponds to an in plane average grain size of at least 200 nm [37].

FL-hBN flakes are prepared via micromechanical cleavage of the bulk hBN on oxidised Si wafers (SiO_2 285 nm thick). After exfoliation, FL-hBN are identified on the Si/SiO_2 substrate by optical contrast. Optical images are acquired using a filter at 580 nm to select the incident wavelength. In these conditions, the optical contrast of 1L-hBN on Si/SiO_2 is highest, ~2%, and it increases linearly with the number of layers. Fig. 1.3a shows the optical contrast of FL-hBN exfoliated on Si/SiO_2 measured under these conditions. ~10%, corresponds to a 5L-BN.

Bulk WSe_2, sourced from HQgraphene, is characterized prior to exfoliation by Raman spectroscopy and PL. The Raman spectrum of bulk WSe_2 is shown in Fig. 1.4a (orange). The main peak at ~250 cm^{-1} is the convolution of the A_{1g} and E_{2g} modes of WSe_2 at ~247 and ~251 cm^{-1} respectively [40], and the shoulder at ~260 cm^{-1} belongs to the 2LA(M) mode [41]. The ~4 cm^{-1} distance between A_{1g} and E_{2g} and the ratio between the intensity of the E_{2g} and 2LA(M) mode, I(E_{2g}-WSe_2)/I(2LA(M) E_{2g}-WSe_2)~1.5, are the crystal. Under these conditions, consistent with the reported spectrum of bulk WSe_2 [40]. PL from bulk WSe_2 crystals is shown in Fig. 1.4b (orange curve). The peak at ~890 nm corresponds to the optical bandgap of bulk WSe_2 [24]. Bulk WSe_2 is then exfoliated by micromechanical cleavage on oxidised silicon wafers (oxide 285 nm thick) following the same procedures as for hBN and graphite. Single-layers are identified via optical contrast using the green channel, as for Fig. 1.3b. The contrast of 1L-WSe_2 is significantly higher than both SLG and hBN, ~25%.

After having exfoliated and identified the separate crystals, the heterostructure is assembled via a dry-transfer technique [35,42]: a transparent stack comprising a glass slide, a polydimethylsiloxane (PDMS) layer (~1-mm thick) attached to the glass and polycarbonate (PC) as external film, of roughly the same size of PDMS, is mounted on a micromanipulator positioned under an optical microscope with a temperature-controlled stage. The materials forming the stack are all transparent, which allows the visualization of the sample below. The Si/SiO_2 substrate supporting the 1L-WSe_2 flake is placed on the stage and is the first to be picked up, as it will form the top layer of the final structure. After adjusting the alignment between the stack and the 1L-WSe_2 crystal, the stage is heated to ~50 °C, then the transfer stack is brought into contact with crystals can be picked up on the stack due

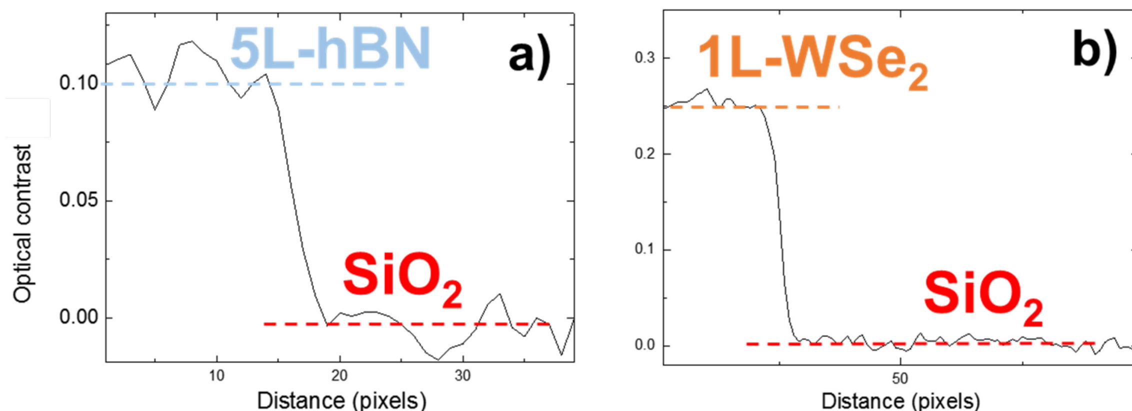

Fig. 1.3 a) optical contrast of 5L-hBN at 580 nm. b) optical contrast of 1L-WSe_2 flake in the green channel. Contrast is ~25%.

to their higher adhesion to PC compared to SiO_2. The substrate is then changed and another Si/SiO_2 substrate with 5L-hBN is placed on the stage. The procedure is repeated: the WSe_2 on PC/PMMS/glass is aligned to the hBN crystal. Then the two crystals are brought in contact and finally 5L-hBN can be picked up to form a 1L-WSe_2/5L-hBN layer on the supporting stack. 1L-WSe_2 and 5L-hBN adhere strongly to each other. When parts of hBN stick out of the WSe_2 layer, the adhesion of 5L-hBN to PC at~50 °C is still enough to pick up the whole stack without damage. Finally, the Si/SiO_2 substrate with the selected SLG flakes is placed on the stage. The 1L-WSe_2/5L-hBN layer on the transfer stack is then aligned to the SLG flake on Si/SiO_2 and all the layers are brought in contact. The temperature is raised to ~100 °C, which ensures adhesion of the whole PC film to SiO_2. The PC can therefore be released from the PDMS/glass. Then, the sample is soaked in chloroform to dissolve the PC film, leaving the final heterostructure. This is then characterised by Raman spectroscopy on different points: on an area comprising only SLG on Si/SiO_2, on an area comprising only 5L-hBN on Si/SiO_2, on an area comprising only 1L-WSe_2 on Si/SiO_2, on an area formed only by 5L-hBN/SLG and on the full 1L-WSe_2/5L-hBN/SLG stack.

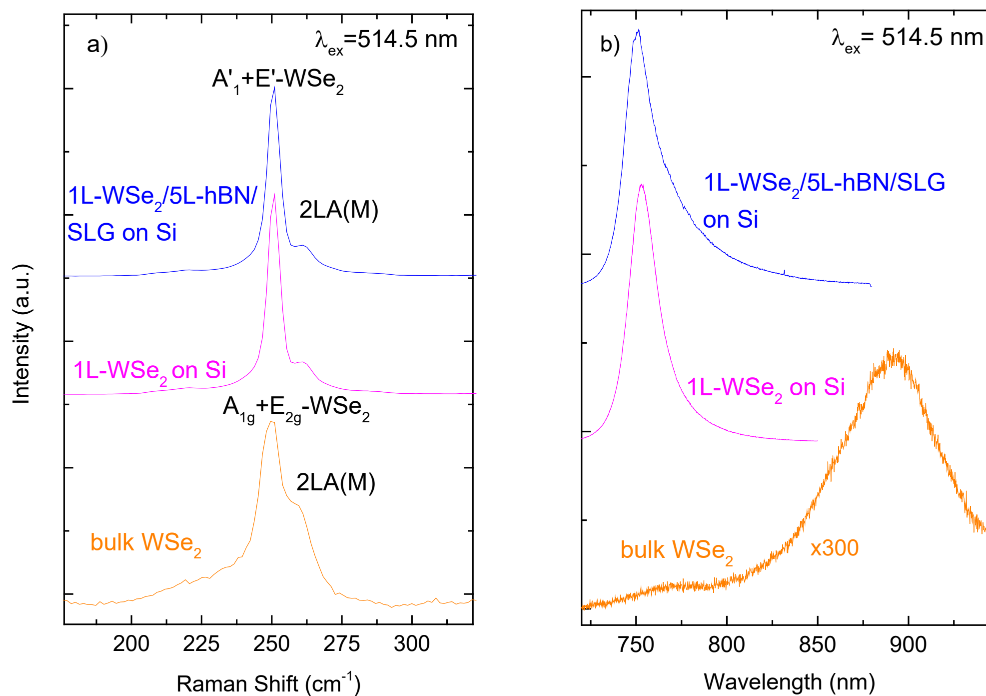

Figure 1.4: Comparison of (a) Raman and (b) PL spectra of 1L-WSe_2 on Si/SiO_2 (pink curve) and 1L-WSe_2/5L-hBN/SLG on Si/SiO_2 (blue curve). Excitation wavelength 514.5 nm.

Fig. 1.2 (black curve), plots the Raman spectrum of a SLG on Si/SiO_2. The G peak corresponds to the high frequency E_{2g} phonon at Γ [43]. The D peak is due to the breathing modes of six-atom rings and requires a defect for its activation [43,44]. It comes from transverse optical (TO) phonons around the Brillouin Zone (BZ) edge K [43], is active by double resonance (DR) [45] and is strongly dispersive with excitation energy due to a Kohn Anomaly (KA) at K [46]. DR can also happen as intra-valley process, i.e. connecting two points belonging to the same cone around K or K'. This gives the so-called D' peak. The 2D peak is the D peak overtone while the 2D' peak is the D' overtone. Since 2D and 2D' originate from a process where

momentum conservation is satisfied by two phonons with opposite wave vectors, no defects are required for their activation, and are thus always present [47]. The 2D peak is a single Lorentzian in SLG, whereas it splits into several components as the number of layers increases, reflecting the evolution of the electronic band structure [48]. The 2D peak in Fig. 1.1b is a single Lorentzian, which confirms the SLG nature of the sample. The position of the G peak, Pos(G), is ~1591 cm^{-1}, its full width at half maximum, FWHM(G), ~8.5 cm^{-1}, Pos(2D) ~2685 cm^{-1}, FWHM(2D)~28.7 cm^{-1}, the intensity ratio between 2D and G peak, I(2D)/I(G), ~1.17 and area ratio, A(2D)/A(G), ~3.9. This allows us to estimate a doping ~0.8x10^{13} cm^{-2}, corresponding to a Fermi level ~370 meV [49]. The absence of D peak indicates negligible defect density [44,50,51].

The Raman spectrum of the 5L-hBN on SiO_2 is shown Fig. 1.2a (red line). The E_{2g} peak is at ~1367.5 cm^{-1}, ~2 cm^{-1} blueshifted compared to the bulk, consistent with what expected from a thinner crystal [37,39], while FWHM (E_{2g}-5L-hBN) is ~10.5 cm^{-1}, 0.1 cm^{-1} higher than the error bar introduced by the resolution of the spectrometer, which corresponds to a grain size ~80 nm [37]. Raman and PL spectra of 1L-WSe_2 on Si/SiO_2 (magenta) are shown in Fig. 1.4. The peak at ~250 cm^{-1} belongs to the A_1' and E' modes [40,41], which are degenerate in 1L-WSe_2 [40]. I(E_{2g}-1L-WSe_2)/I(2LA(M)-1L-WSe_2) increases to ~10, consistent with a low number of layers[40]. The absence of the $A^2{}_{1g}$ mode at ~310 cm^{-1} is also consistent with this being 1L-WSe_2 [41], however it is not advisable to use the absence of a peak as a characterization tool, because one can never be sure why something is absent [34]. So the thickness is further confirmed by PL (Fig. 1.4b, magenta), where a single peak arises at ~750 nm, blueshifted ~140 nm compared to bulk WSe_2. This is due to emission from the A exciton, corresponding to the direct transition between top conduction and bottom valence band at the K and K' points [24]. The peak of 1L-WSe_2 is ~2 orders of magnitude more intense compared to the bulk crystal. No other peaks in the 800-900 nm region are seen, which would be a signature of indirect bandgap transitions of a larger number of layers [24].

Fig. 1.1 (green curve) plots the Raman spectrum of 5L-hBN on SLG. Pos(G) is ~1590 cm^{-1}, FWHM(G) ~8.2 cm^{-1}, Pos(2D) ~2694 cm^{-1} , FWHM(2D) ~24.4 cm^{-1}, I(2D)/I(G) ~1.53 and A(2D)/A(G) ~4.5. We observe a ~9 cm^{-1} upshift in Pos(2D) compared to the SLG on SiO_2 case, while the G peak is downshifted by ~1 cm^{-1}. From these values we derive a doping ~0.3 x$10^{13}$$cm^{-2}$, reduced compared to the case of SLG on Si/SiO_2. The reduction in doping can be explained by the 5L-hBN flake covering the SLG. 5L-hBN is not only protecting SLG from the ambient air and moisture, which contribute to p-doping, but also removes moisture or other residuals on top of SLG due to a self-cleaning process [52]. Pos (E_{2g}-5L-hBN) ~1367.5 cm^{-1} and FWHM (E_{2g}-5L-hBN) ~11 cm^{-1} show no significant changes compared to the spectrum of 5L-hBN on Si/SiO_2. The D peak is absent implying no defects are introduced in SLG after placing 5L-hBN on top.

The Raman spectrum of the 1L-WSe_2/5L-hBN/SLG heterostructure is shown in Figs.1.2 and S1.4 (blue curves). All peaks belonging to the separate materials can be identified in the spectrum. We find Pos(G) ~1590 cm^{-1}, FWHM(G) ~8.7 cm^{-1}, Pos(2D) ~2695 cm^{-1}, FWHM(2D) ~26.2 cm^{-1}, I(2D)/I(G) ~1.58 and A(2D)/A(G) ~4.7. These values are analogous to the case of 5L-hBN on SLG and correspond to a doping of ~0.3 x10^{12} cm^{-2}. The D peak (Fig. 1.1a) is still absent, implying no defects are introduced in SLG from the stacking of the layers. Pos(E_{2g}-5L-hBN) ~1367.5 cm^{-1}, while FWHM (E_{2g}-5L-hBN) ~10.5 cm^{-1}, implying no

significant change in the spectrum of 5L-hBN on SLG after adding 1L-WSe_2. From the analysis of the Raman spectrum of 1L-WSe_2 on top of the stack (Fig. S1.4a), pos(A_1'+E'-1L-WSe_2) ~250 cm^{-1}, unchanged compared to the values measured on Si/SiO_2. The B exciton of 1L-WSe_2 at ~610 nm is responsible for PL background in the ~3000 cm^{-1} region of the Raman spectrum [24].

The PL spectrum of the heterostructure is shown in Fig. S1.4b. The position of the A exciton remains unchanged at ~752 nm compared to the case of 1L-WSe_2 on SiO_2.

In order to confirm the thickness of the 5L-hBN layer, AFM measurements are performed once the optical characterisation is concluded. Fig 1.5 shows the AFM measurements of the hBN identified by optical contrast to be ~5 layers thick, on a step formed by 5L-hBN on SiO_2. The thickness is ~2.4 nm. We measure the hBN interlayer step to be ~0.38 nm, which would imply a ~6 layers. However, under ambient conditions, 2d crystals on SiO_2 have been measured to be thicker than that expected by multiplying the number of layers by the interlayer distance [53]. This discrepancy is assigned the presence of a gaseous species or water intercalating between the SiO_2 and the crystal [53]. In our case, a 5L-hBN crystal should have a thickness~2 nm according to its interlayer distance, but we assume the extra ~0.5 nm to be due to the aforementioned increase in the thickness caused by the presence of contaminations.

1.2 WS_2/hBN/SLG heterostructures

The second set of devices are assembled and characterised as follows.

HOPG sourced from NGS Naturgrafit is exfoliated by means of micromechanical cleavage following the same procedure described in Section S1.1. SLG flakes are again identified on Si/SiO_2 by optical contrast, see Fig. 1.6a.

hBN is sourced and exfoliated as described in S1.1. After exfoliation, FL-hBN flakes are identified on the Si/SiO_2 by optical contrast. Fig. 1.6b shows the contrast of the flake on Si/SiO_2 chosen for

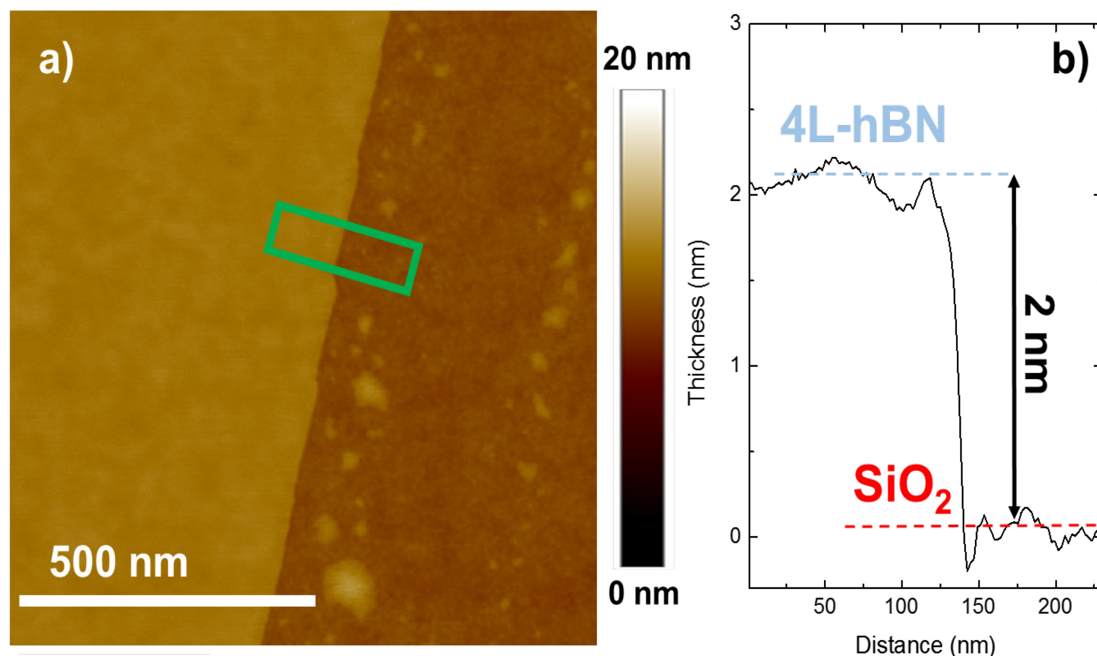

Figure 1.5: a) AFM image of hBN on SiO_2. The image is acquired after the fabrication of the heterostructure. The green rectangle shows the region where the step is measured; b) Step height in the green area, corresponding to a thickness ~2.4 nm.

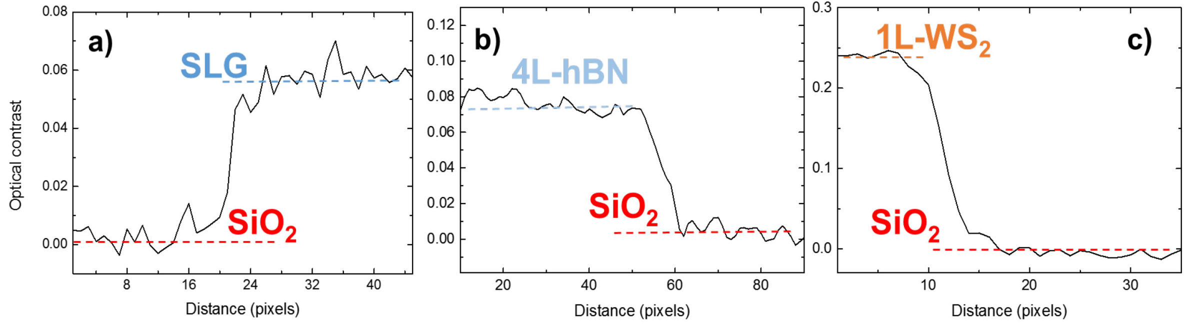

Fig. 1.6 a) SLG, with optical contrast ~5.5%; b) 4L-hBN, with optical contrast ~7.4%, c) 1L-WS_2, with contrast ~24%.

this device assembly, which is ~7.4%, corresponding to a 4L.

Bulk WS_2 is characterised by Raman and PL spectroscopy. The Raman spectrum of bulk WS_2 is shown in Fig. 5.4a (orange curve). The most prominent peaks at ~350 and ~420 cm^{-1} are assigned to the 2LA(M) and A_{1g} modes of WS_2 [54]. At 514.5 nm, the ratio between the peaks, I(2LA(M)-WS_2)/I(A_{1g}-WS_2), is a function of the number of layers and is expected to increase with decreasing number of layers [54]. In the case of bulk WS_2 the ratio is ~0.6. The PL spectrum of bulk WS_2 is shown by the orange curve, with a peak corresponding to the optical bandgap at ~640 nm. Bulk WS_2 is exfoliated on Si/SiO_2 using the same procedure as described in Section 1.1. 1L-WS_2 crystals are identified by optical contrast, as shown in Fig. 1.6c, where we measure a monolayer contrast ~24%.

After having exfoliated and identified the separate crystals, the heterostructure is assembled via dry-transfer with the same procedure described in S1.1.

Once the fabrication is complete, we characterise by Raman spectroscopy first the areas with the separate crystals on Si/SiO_2, then an area with 4L-hBN/SLG and finally the full stack comprising 1L-WS_2/4L-hBN/SLG. PL is also employed to further characterise WS_2 both on SiO_2 and on the heterostructure.

Fig. 1.7 (black curve), plots the Raman spectrum of SLG on Si/SiO_2. The 2D peak is a single Lorentzian, which confirms the SLG nature of the sample. Pos(G) ~1591 cm^{-1}, FWHM(G) ~11.5 cm^{-1}, Pos(2D) ~2687 cm^{-1}, FWHM(2D)~31.1 cm^{-1}, I(2D)/I(G), ~1.6 and A(2D)/A(G),

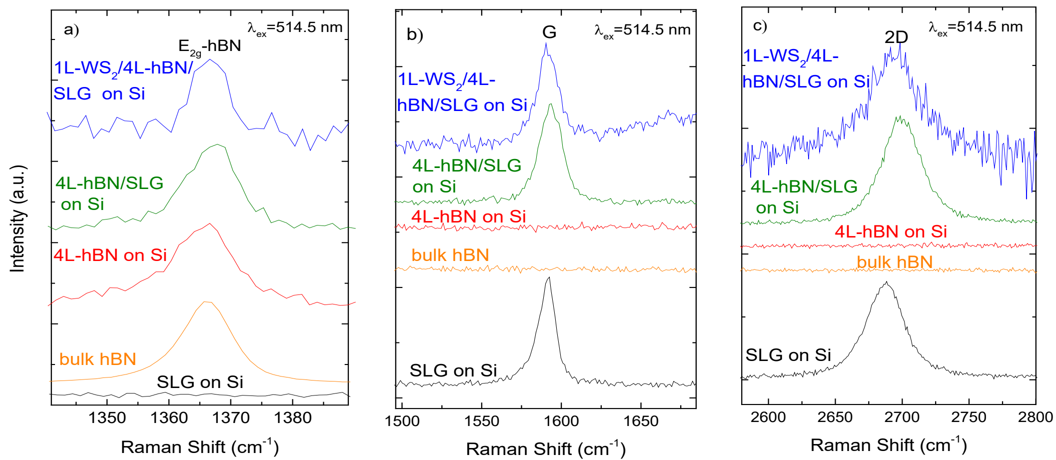

Figure 1.7: Raman spectra of SLG on Si/SiO_2 (black curve), 4L-hBN on Si/SiO_2 (red curve), 4L-hBN/SLG (green curve), and 1L-WS_2/4L-hBN/SLG (blue curve).

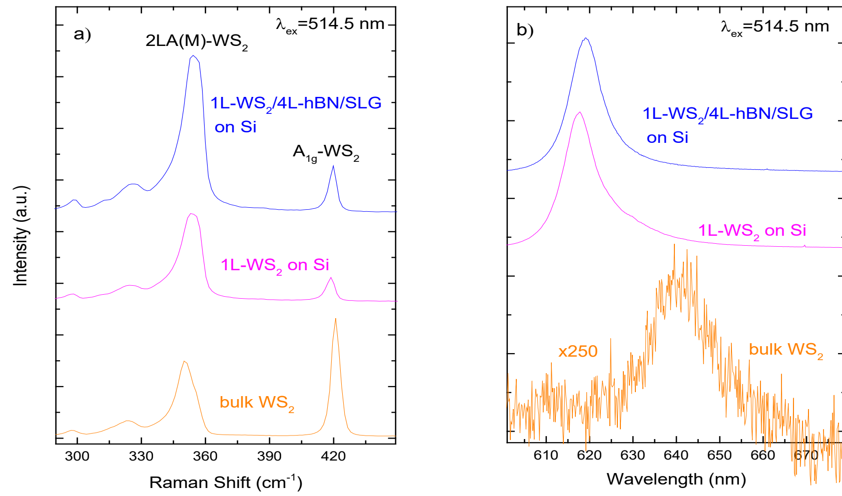

Figure 1.8: Comparison of (a) Raman and (b) PL spectra of bulk WS_2 (orange curve), of 1L-WS_2 on Si/SiO_2 (pink curve) and of 1L-WS_2/4L-hBN/SLG on Si/SiO_2 (blue curve).

~4.4 indicate doping ~0.5×10^{13}. The absence of a D peak indicates negligible defects. The Raman spectrum of the 4L-hBN on Si/SiO_2 is shown in Fig. 1.7a (red curve). Pos (E_{2g}-4L-hBN) is ~1367 cm^{-1}, ~1.5 cm^{-1} blueshifted compared to the bulk crystal and consistent with a low number of layers [39]. FWHM (E_{2g}-4L-hBN)~9.3 cm^{-1} is analogous to the bulk crystal and corresponds to a grain size >200 nm. The Raman spectrum of 1L-WS_2 on Si/SiO_2 is shown in Fig. 1.8a (pink curve). The 2LA(M) and A_{1g} modes are respectively at ~353 and ~419 cm^{-1}. I(2LA(M)-1L-WS_2)/I(A_{1g}-1L-WS_2) is ~2.6, over 4 times higher compared to the bulk case (~0.6). This is a signature of a monolayer, because a 2L-WS_2 is expected to have I(2LA(M)-2L-WS_2)/I(A_{1g}-2L-WS_2) ~1 [54]. In order to further confirm the thickness of the exfoliated 1L-WS_2, its PL spectrum is acquired, Fig. 1.7b (pink curve). The main feature at ~618 nm, ~20 nm blueshifted compared to the bulk case, corresponds to emission from the A exciton, corresponding to the direct optical bandgap between the top valence and the bottom conduction band of 1L-WS_2. Furthermore, the intensity is ~250 times higher compared to the bulk case, as expected [24].

Fig. 1.7 (green curve) plots the Raman spectrum of 4L-hBN on SLG. Pos(G) ~1593 cm^{-1}, FWHM(G) ~14.5 cm^{-1}, Pos(2D) ~2699.5 cm^{-1}, FWHM(G)~14.5 cm^{-1}, I(2D)/I(G), ~1.91

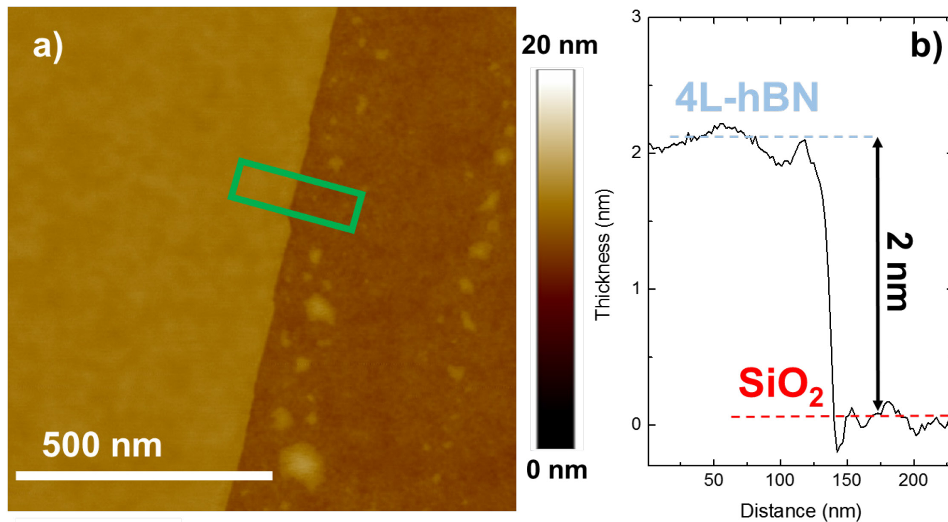

Figure 1.9: a) AFM image of hBN on SiO_2. The green rectangle shows the region where the step is measured; b) Step height corresponding to the area included by the green rectangle.

and A(2D)/A(G) ~4.45. This indicates doping~0.4x10^{13}. No D peak is seen. Pos (E_{2g}-4L-hBN) ~1365.5 cm^{-1}, FWHM(E_{2g}-4L-hBN) is ~11.8 cm^{-1}, ~2.5 cm^{-1} broader compared to the case of 4L-hBN on SLG, indicating a smaller grain size.

We then perform Raman and PL characterisation on the whole 1L-WS_2/4L-hBN/SLG heterostructure, as shown in Figs. 1.7 and 1.8 (blue curves). Pos(G) ~1591.5 cm^{-1}, FWHM(G) ~15.3 cm^{-1}, Pos(2D) ~2693.5 cm^{-1}, FWHM(2D) ~38.5 cm^{-1}, I(2D)/I(G) ~1.9 and A(2D)/A(G) ~2.3. This indicates doping~0.3x10^{13}. Pos (E_{2g}-4L-hBN) ~1366.5 cm^{-1}, and FWHM(E_{2g}-4L-hBN) ~11 cm^{-1}. Pos(2LA(M)-WS_2) ~353 cm^{-1}, Pos(A_{1g}-WS_2) ~419 cm^{-1}, with no change compared to 1L-WSe_2 characterised on Si/SiO_2. Figure 1.8b, blue line, shows the PL spectrum of the 1L-WS_2/4L-hBN/ SLG heterostructure. The A exciton at ~619 nm is nearly unchanged compared to the PL spectrum of 1L-WS_2 on Si/SiO_2.

As a last step we perform AFM characterisation to confirm the thickness derived from optical contrast, as shown in Fig. 1.9. The step between 4L-hBN and SiO_2 is ~2 nm. As discussed in Section S1.1, considering an interlayer distance ~0.38 nm and an increase in thickness due to the effect of the environment ~0.5 nm, we conclude that the flake is a 4L-hBN.

2. Current-voltage characteristics of WSe_2 and WS_2-based QLED devices

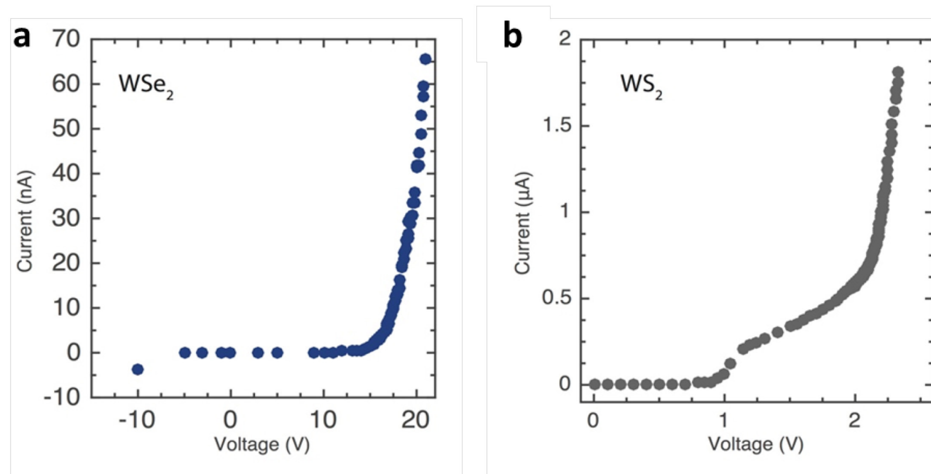

Figure 2: Current vs. Voltage measurements taken at 10 K from (a) 1L-WSe_2 (a) and (b) 1L-WS_2 -based QLEDs. A negative bias applied to the SLG raises its E_F and allows electrons to tunnel into the conduction band of WSe_2, increasing the current. Similarly for the WS_2 device, by lowering the SLG E_F with a positive bias, holes can tunnel into the WS_2 valence band. The step in the I-V curve in panel b is assigned to the different current thresholds of the two 1L-WS_2 flakes present in this specific device.

3. Quantum Optical Measurements

PL and EL measurements are performed using a home-built confocal microscope mounted on a three-axis stage (Physik Instrumente M-405DG) with a 5-cm travel range and 200-nm resolution for coarse alignment and a piezo scanning mirror (Physik Instrumente S-334) for high resolution raster scans. PL and EL are collected using a 1.7-mm working distance objective with a numerical aperture of 0.7 (Nikon S Plan Fluor 60x) and detected on a fibre-coupled single-photon-counting module (PerkinElmer: SPCM-AQRH). A variable-temperature helium flow cryostat (Oxford Instruments Microstat HiRes2) is use to perform PL and EL measurements. A controlled bias is applied to the QLED devices by a source measurement unit (Keithley 2400) for EL experiments. Intensity correlations from the Hanbury Brown and Twiss interferometer are recorded with a time-to-digital converter (quTAU). A double grating spectrometer (Princeton Instruments) is used for acquiring spectra. For PL measurements, the excitation laser (700 nm / 520 nm, Thorlabs MCLS1) is suppressed with a long pass filter (715 nm, Semrock FF01-715 / 550 nm Thorlabs FEL0550). A schematic of the setup is shown in Fig. 3.

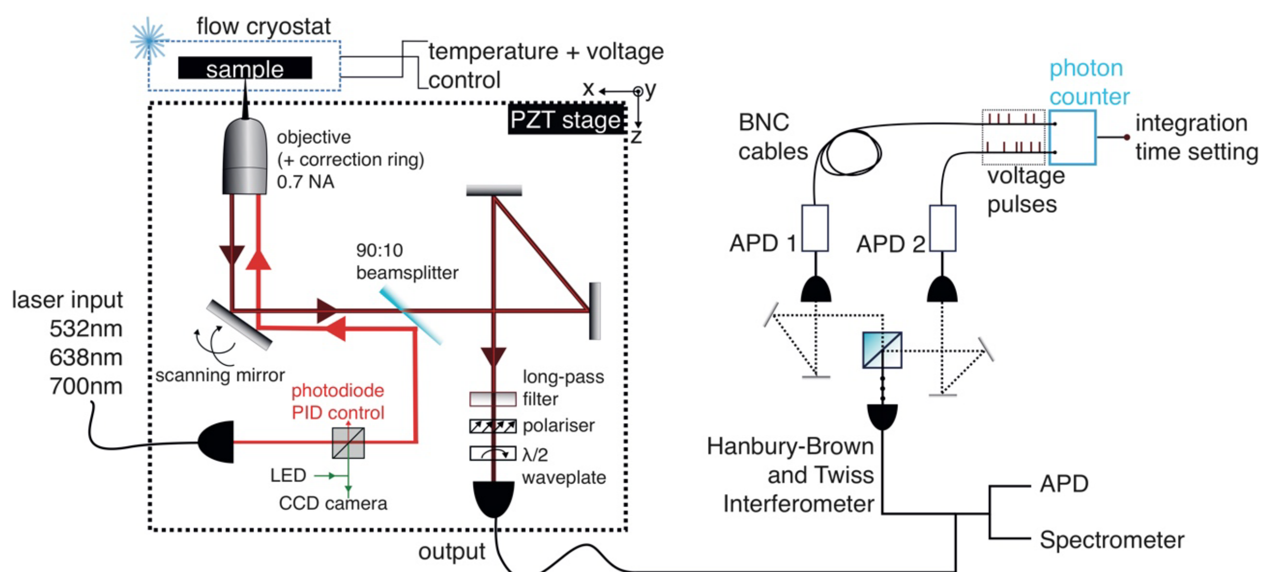

Figure 3: Diagram of the quantum optical measurement setup. A home-built confocal microscope (left, enclosed by dashed lines) is used to obtain micrometre-resolved PL and EL maps. Different laser inputs are used: 638 and 700 nm for 1L and 2L-WSe_2 and 532 nm for 1L-WS_2. The charge-coupled device (CCD) camera and LED allow wide field illumination of the sample to facilitate locating the QLED on the substrate. The light output is either sent to a spectrometer or to an avalanche photodiode (APD) for PL and EL scans. For photon-correlation measurements, the output is sent to a Hanbury Brown and Twiss interferometer [55], *where it is split by a 50:50 beam-splitter and two APDs. The signal from these detectors is correlated using the time-to-digital converter.*

4. Comparison of monolayer and bilayer EL emission for WSe_2-based LED

One of the WSe_2-based QLED devices had an upper contact to both a monolayer and bilayer region in parallel. PL and EL maps of this device are shown in Fig. 4 a) and b) respectively. Interestingly, current is injected preferentially through the bilayer region, and as a result only this region lights up in EL. In contrast, the monolayer region is brighter than the bilayer in PL.

5. Spectral wandering and blinking QLED spectra

The narrowest linewidths observed from the 1L and 2L-WSe_2-based devices are 1 nm, in contrast to those seen under PL ~0.05 nm. Measurements of the electrically driven single emitters over time show a spectral wandering ~2 nm, compared to ~0.5 – 1 nm under PL. Under EL these emitters blink at timescales of seconds, as shown in Fig. 5. There appears to be no blinking at the sub-millisecond timescale. However, we observe no bunching in the photon correlation measurements, as reported previously for PL experiments on 1L and FL-WSe_2 quantum emitters [12–16]. Spectral measurements over time of the electrically driven 1L-WS_2 emitters indicate that the spectral wandering cannot be well resolved due to a broader linewidth ~4 nm.

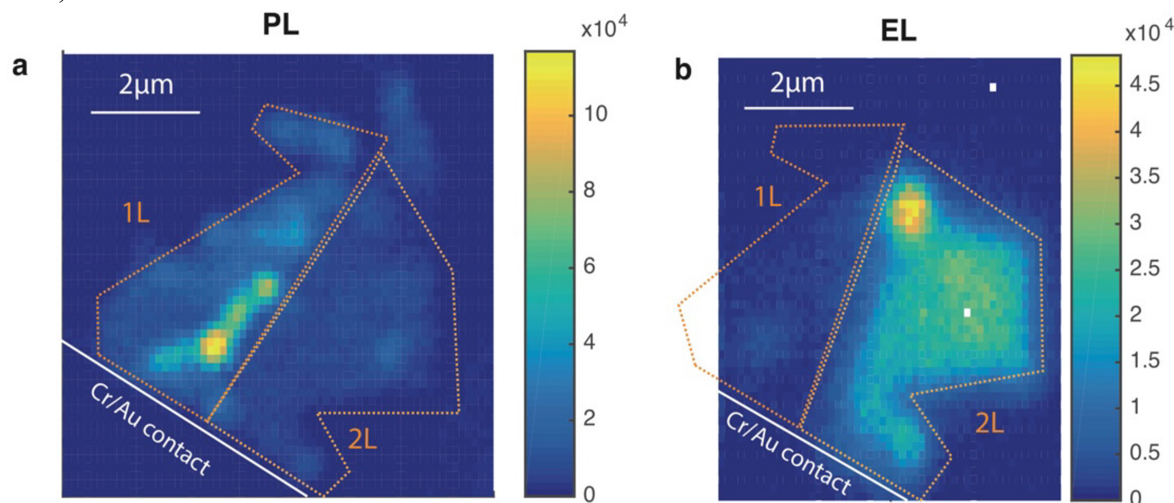

Figure 4: Maps of one of the WSe_2-based QLED devices taken at 10 K, showing a 1L and a 2L region which appear brighter in (a) PL and (b) EL maps respectively.

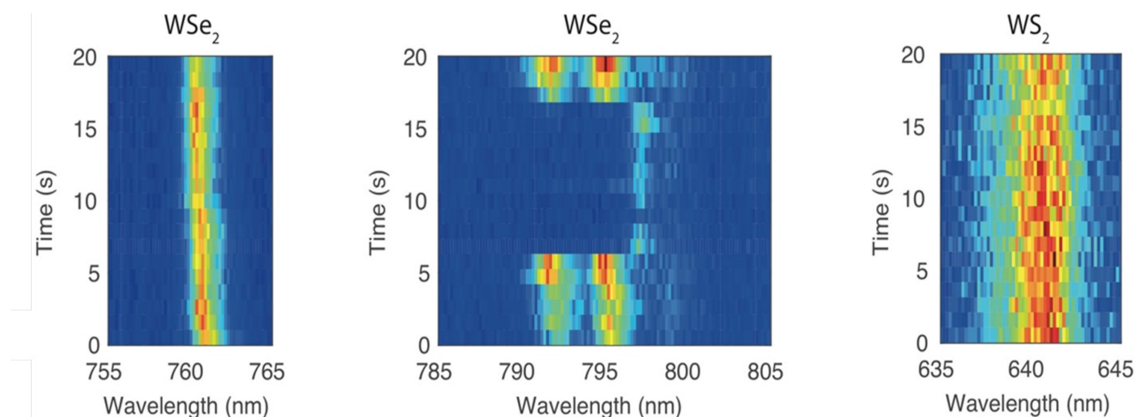

Figure 5: Spectral wandering measurements of electrically-driven quantum emitters taken at 10K with a time resolution of 1s per spectra.

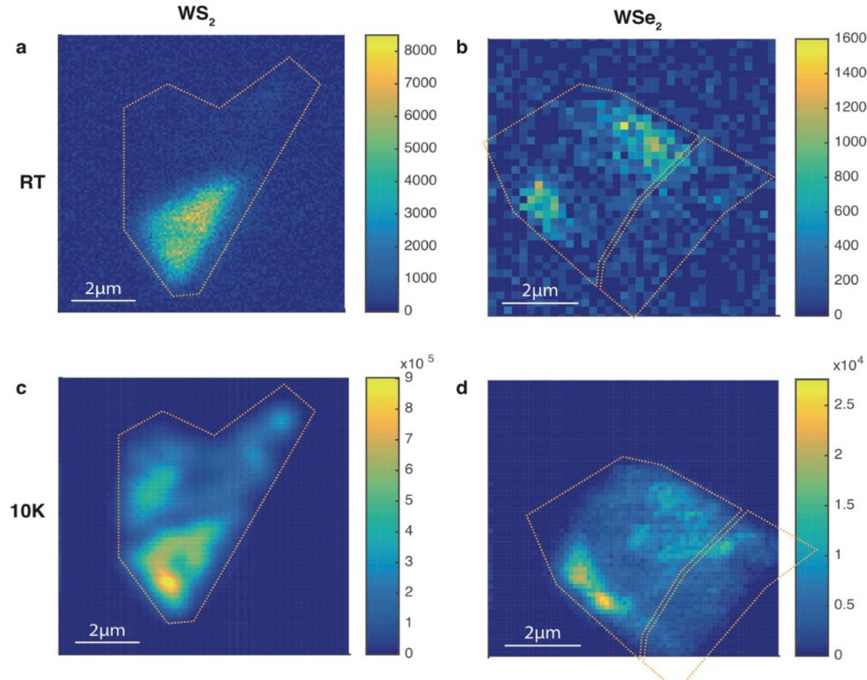

Figure 6: EL maps at RT and 10K of the WSe_2 and WS_2 LED devices. (a) 665 nA (1.992 V) and (c) at 665 nA (2.08 V). (b) 200 nA (-2 V) and (d) 900 nA (-3.2 V).

6. Temperature-dependent EL maps

An increase of several orders of magnitude is observed in unbound exciton EL when lowering the temperature from RT to 10 K: a 4-fold increase is measured in the 1L- and 2L-WSe_2-based LED and a ~100-fold increase in the 1L-WS_2 device as shown in Figure 6.

7. Comparison of low temperature PL and EL spectra for WS_2-based QLED

Fig. 7 compares the spectra taken in EL and PL at 10K from the 1L-WS_2-based QLED, at the site were single-photon emission is seen. The PL spectrum comprises multiple peaks, while the EL is narrow and predominantly a single peak. This may be due to generation of multiple exciton complexes as well as other donor-based delocalised emission from WS_2.

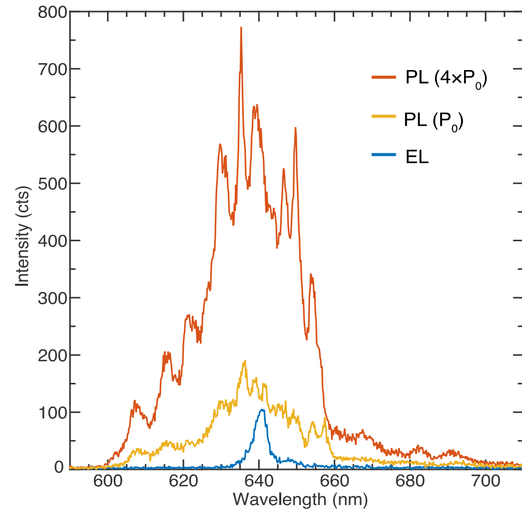

Figure 7: EL and PL from the 1L-WS_2-based device at the location where single-photon emission is observed. P_0 is 225 nW for the PL spectra and the injected current is 5754 nA (1.985 V) for the EL spectrum.

REFERENCES

[1] Z. Yuan, B.E. Kardynal, R.M. Stevenson, A.J. Shields, C.J. Lobo, K. Cooper, et al., Science. 295 (2002) 102–105.

[2] N. Mizuochi, T. Makino, H. Kato, D. Takeuchi, M. Ogura, H. Okushi, et al., Nat. Photonics. 6 (2012) 299–303.

[3] A. Lohrmann, N. Iwamoto, Z. Bodrog, S. Castelletto, T. Ohshima, T.J. Karle, et al., Nat. Commun. 6 (2015) 7783.

[4] F. Bonaccorso, Z. Sun, T. Hasan, A.C. Ferrari, Nat. Photonics. 4 (2010) 611–622.

[5] A.C. Ferrari, Nanoscale. 7 (2014) 4598–4810.

[6] Y. Ye, Z.J. Wong, X. Lu, X. Ni, H. Zhu, X. Chen, et al., Nat. Photonics. 9 (2015) 733–737.

[7] Z. Sun, T. Hasan, F. Torrisi, D. Popa, G. Privitera, F. Wang, et al., ACS Nano. 4 (2010) 803–810.

[8] M. Liu, X. Yin, E. Ulin-Avila, B. Geng, T. Zentgraf, L. Ju, et al., Nature. 474 (2011) 64–67.

[9] C.T. Phare, Y.-H. Daniel Lee, J. Cardenas, M. Lipson, Nat. Photonics. 9 (2015) 511–514.

[10] F.H.L. Koppens, T. Mueller, P. Avouris, A.C. Ferrari, M.S. Vitiello, M. Polini, Nat. Nanotechnol. 9 (2014) 780–793.

[11] F. Xia, H. Wang, D. Xiao, M. Dubey, A. Ramasubramaniam, Nat. Photonics. 8 (2014) 899–907.

[12] A. Srivastava, M. Sidler, A. V. Allain, D.S. Lembke, A. Kis, A. Imamoğlu, Nat. Nanotechnol. 10 (2015) 491–496.

[13] Y.-M. He, G. Clark, J.R. Schaibley, Y. He, M.-C. Chen, Y.-J. Wei, et al., Nat. Nanotechnol. 10 (2015) 497–502.

[14] C. Chakraborty, L. Kinnischtzke, K.M. Goodfellow, R. Beams, A.N. Vamivakas, Nat. Nanotechnol. 10 (2015) 507–511.

[15] M. Koperski, K. Nogajewski, A. Arora, V. Cherkez, P. Mallet, J.-Y. Veuillen, et al., Nat. Nanotechnol. 10 (2015) 503–506.

[16] P. Tonndorf, R. Schmidt, R. Schneider, J. Kern, M. Buscema, G.A.R.Y.A.S. Steele, et al., Optica. 2 (2015) 347.

[17]T.T. Tran, K. Bray, M.J. Ford, M. Toth, I. Aharonovich, Nat. Nanotechnol. 11 (2015) 37–41.

[18] Z. Yin, H. Li, H. Li, L. Jiang, Y. Shi, Y. Sun, et al., ACS Nano. 6 (2011) 74–80.

[19] H. Wang, C. Zhang, W. Chan, S. Tiwari, F. Rana, Nat. Commun. 6 (2015) 8831.

[20] J.S. Ross, P. Klement, A.M. Jones, N.J. Ghimire, J. Yan, D.G. Mandrus, et al., Nat. Nanotechnol. 9 (2014) 268–272.

[21] B.W.H. Baugher, H.O.H. Churchill, Y. Yang, P. Jarillo-Herrero, Nat. Nanotechnol. 9 (2014) 262–267.

[22] A. Pospischil, M.M. Furchi, T. Mueller, Nat. Nanotechnol. 9 (2014) 257–261.

[23] F. Withers, O. Del Pozo-Zamudio, A. Mishchenko, A.P. Rooney, A. Gholinia, K. Watanabe, et al., Nat. Mater. 14 (2015) 301–306.

[24] B. Zhou, L.X. Yang, F. Chen, M. Xu, T. Wu, G. Wu, et al., ACS Nano. 7 (2013) 791–797.

[25] A.M. Jones, H. Yu, N.J. Ghimire, S. Wu, G. Aivazian, J.S. Ross, et al., Nat. Nanotechnol. 8 (2013) 634–638.

[26] G. Wang, L. Bouet, D. Lagarde, M. Vidal, A. Balocchi, T. Amand, et al., Phys. Rev. B. 90 (2014).

[27] S. Kumar, A. Kaczmarczyk, B.D. Gerardot, Nano Lett. 15 (2015) 7567–7573.

[28] M.D. Eisaman, J. Fan, A. Migdall, S. V Polyakov, Rev. Sci. Instrum. 82 (2011) 071101.

[29] R. Warburton, C. Schaflein, D. Haft, F. Bickel, a Lorke, K. Karrai, et al., Nature. 405 (2000) 926–9.

[30] K.C. Nowack, F.H.L. Koppens, Y. V Nazarov, L.M.K. Vandersypen, Science. 318 (2007) 1430–1433.

[31] C.L. Salter, R.M. Stevenson, I. Farrer, C.A. Nicoll, D.A. Ritchie, A.J. Shields, Nature. 465 (2010) 594–597.

[32] K. Watanabe, T. Taniguchi, H. Kanda, Nat. Mater. 3 (2004) 404–409.

[33] C. Casiraghi, A. Hartschuh, E. Lidorikis,

H. Qian, H. Harutyunyan, T. Gokus, et al., Nano Lett. 7 (2007) 2711–2717.

[34] A.C. Ferrari, D.M. Basko, Nat. Nanotechnol. 8 (2013) 235–246.

[35] F. Bonaccorso, A. Lombardo, T. Hasan, Z. Sun, L. Colombo, A.C. Ferrari, Mater. Today. 15 (2012) 564–589.

[36] K.S. Novoselov, D. Jiang, F. Schedin, T.J. Booth, V. V Khotkevich, S. V Morozov, et al., Proc. Natl. Acad. Sci. U. S. A. 102 (2005) 10451–3.

[37] R.J. Nemanich, S.A. Solin, R.M. Martin, Phys. Rev. B. 23 (1981) 6348–6356.

[38] S. Reich, A.C. Ferrari, R. Arenal, A. Loiseau, I. Bello, J. Robertson, Phys. Rev. B. 71 (2005) 205201.

[39] R. Arenal, A.C. Ferrari, S. Reich, L. Wirtz, J.-Y. Mevellec, S. Lefrant, et al., Nano Lett. 6 (2006) 1812–6.

[40] H. Terrones, E. Del Corro, S. Feng, J.M. Poumirol, D. Rhodes, D. Smirnov, et al., Sci. Rep. 4 (2014) 4215.

[41] W. Zhao, Z. Ghorannevis, K.K. Amara, J.R. Pang, M. Toh, X. Zhang, et al., Nanoscale. 5 (2013) 9677–83.

[42] P.J. Zomer, M.H.D. Guimarães, J.C. Brant, N. Tombros, B.J. van Wees, Appl. Phys. Lett. 105 (2014) 013101.

[43] F. Tuinstra, Raman Spectrum of Graphite, J. Chem. Phys. 53 (1970) 1126.

[44] A.C. Ferrari, J. Robertson, Phys. Rev. B. 61 (2000) 14095–14107.

[45] C. Thomsen, S. Reich, Phys. Rev. Lett. 85 (2000) 5214–7.

[46] S. Piscanec, M. Lazzeri, F. Mauri, A.C. Ferrari, J. Robertson, Phys. Rev. Lett. 93 (2004) 185503.

[47] D.M. Basko, S. Piscanec, A.C. Ferrari, Phys. Rev. B. 80 (2009) 165413.

[48] A.C. Ferrari, J.C. Meyer, V. Scardaci, C. Casiraghi, M. Lazzeri, F. Mauri, et al., Phys. Rev. Lett. 97 (2006) 187401.

[49] A. Das, S. Pisana, B. Chakraborty, S. Piscanec, S.K. Saha, U. V Waghmare, et al., Nat. Nanotechnol. 3 (2008) 210–215.

[50] M. Bruna, A.K. Ott, M. Ijäs, D. Yoon, U. Sassi, A.C. Ferrari , ACS Nano. 8 (2014) 7432–41.

[51] L.G. Cançado, A. Jorio, E.H.M. Ferreira, F. Stavale, C.A. Achete, R.B. Capaz, et al., Nano Lett. 11 (2011) 3190–3196.

[52] S.J. Haigh, A. Gholinia, R. Jalil, S. Romani, L. Britnell, D.C. Elias, et al., Nat. Mater. 11 (2012) 764–7.

[53] M. Ishigami, J.H. Chen, W.G. Cullen, M.S. Fuhrer, E.D. Williams, Nano Lett. 7 (2007) 1643–8.

[54] A. Berkdemir, H.R. Gutiérrez, A.R. Botello-Méndez, N. Perea-López, A.L. Elías, C.-I. Chia, et al., Sci. Rep. 3 (2013) 1755..

[55] R. Hanbury Brown, R.Q. Twiss, A Nature. 178 (1956) 1046–1048.

---

*Electronic address:ma424@cam.ac.uk
†Electronic address: acf26@cam.ac.uk